Progress in Oceanography 227 (2024) 103312

Contents lists available at ScienceDirect

Progress in Oceanography

journal homepage: www.elsevier.com/locate/pocean

Dynamic population modeling of bacterioplankton community response to gelatinous marine zooplankton bloom collapse and its impact on marine nutrient balance

Filip Strniša [a,*], Tinkara Tinta [b,c], Gerhard J. Herndl [c,d,e], Gregor Kosec [a]

[a] Parallel and Distributed Systems Laboratory, Jožef Stefan Institute, Ljubljana, Slovenia
[b] Marine Biology Station Piran, National Institute of Biology, Piran, Slovenia
[c] Department of Functional and Evolutionary Ecology, Bio-Oceanography and Marine Biology Unit, University of Vienna, Vienna, Austria
[d] Department of Marine Microbiology and Biogeochemistry, NIOZ, Royal Netherlands Institute for Sea Research, Den Burg, The Netherlands
[e] Vienna Metabolomics & Proteomics Center, University of Vienna, Vienna, Austria

ARTICLE INFO

Dataset link: https://gitlab.com/e62Lab/public/2024_p_jellyfish_decay_example_code

Keywords:
Jellyfish detritus
von Foerster equation
Kill-the-winner
Nutrient release
Marine bacteria
Modeling

ABSTRACT

The diverse microbial community in the ocean, encompassing various metabolic types, interacts with the wide array of compounds in the dissolved organic matter (DOM) pool, thereby influencing the ocean's biogeochemical state and, consequently, the global climate. Our understanding of the interactions between specific DOM constituents and microbial consortia remains limited, necessitating further refinement to achieve a mechanistic comprehension of the relationship between the DOM field and the microbial metabolic network. Attaining this level of understanding is crucial for accurately predicting the marine ecosystem's response to natural and anthropogenic perturbations. To address this gap, we developed a bacterial population model based on the von Foerster equation. This model aims to describe the complex microbial-mediated degradation of gelatinous zooplankton (hereinafter 'jellyfish') detritus, as an important, but largely overlooked source of DOM in the ocean. By considering microbial growth and decay, as well as DOM uptake, and nutrient release, the model is able to describe the microbial community's life cycle, and the biochemical transformations of the jellyfish-derived organic matter. We fitted the model to results of laboratory microcosm experiments conducted to simulate scenarios experienced by ambient microbiomes during decay of two different jellyfish species in the northern Adriatic Sea. By interpreting the fitted parameters, we highlight the differences in the microbial response to different jellyfish species, namely how these affect the microbial community composition and the release of nutrients. This model has been specifically designed for integration with ocean circulation models to create a comprehensive physical-biogeochemical ocean model. Such an extended model can be utilized for multi-scale simulations to assess the system's response to jellyfish and jellyfish-derived organic matter. Given that jellyfish blooms may become more prevalent under future ocean scenarios, this modeling approach is essential for understanding their potential impact on marine ecosystems.

1. Introduction

Due to their unique features and metabolic machinery, diverse marine microbes are capable of accessing the plethora of compounds comprising the dissolved organic matter pool (DOM) in the ocean (Azam and Malfatti, 2007). By controlling the uptake, degradation and remineralization of DOM compounds marine microbes contribute to the fate of this largest reservoir of carbon in the biosphere (Hansell et al., 2009). Besides, by returning recycled inorganic nutrients to primary producers, marine microbes crucially contribute to the net CO_2 removal from, and oxygen input to, the atmosphere (Arndt et al., 2013). Thus, a mechanistic understanding of microbial degradation of diverse pools of DOM at different spatial–temporal scales in the ocean is a crucial step towards the comprehension of the global carbon cycle (Shang, 2023). Yet knowledge on the microbial processes and mechanism that governs the degradation of the individual compounds within the oceanic DOM pool is still in its infancy.

The process of microbial degradation of specific organic matter pool is complex and determined by quality and quantity of available substrate and ability of diverse microbes to access and use available compounds for their growth. To reveal the complex relationships between all involved players and components the power of biological

* Corresponding author.
E-mail address: filip.strnisa@ijs.si (F. Strniša).

https://doi.org/10.1016/j.pocean.2024.103312
Received 27 February 2024; Received in revised form 8 July 2024; Accepted 12 July 2024
Available online 18 July 2024

modeling based on mathematical description of microbial-mediated processes in a prototyping environment can be exploited (e.g., for marine sediments Arndt et al., 2013, and references therein and Shang, 2023). By simplifying the complexity of the system, models can also provide an important platform for testing hypotheses and different scenarios, e.g., before staring cumbersome experimental work. Modeling has been used to describe microbial growth and evaluate the factors influencing it (reviewed in McMeekin et al., 2002; McKellar and Lu, 2003; Li et al., 2007; Peleg and Corradini, 2011). Model complexity can further range from including one factor, such as a simple substrate dependency, to more bio-physicochemical processes, environmental conditions, and even biotic interactions (Esser et al., 2015). Microbial growth models are critical components of ocean ecosystem models that link the supply of organic and inorganic resources to the microbial communities, enabling predictions of biomass distributions, resource contributions to food webs, and biogeochemical fluxes. Modeling of bacterial growth in ecology usually makes use of the Monod equation to predict bacterial growth kinetics, and exponential decay functions are used to model bacterial decay (Wade et al., 2016). The Monod model can be improved by the use of population models, such as the von Foerster equation (M'Kendrick, 1925; von Foerster et al., 1960). By assuming the age or maturity dependence of the population (Stukalin et al., 2013; Rochman et al., 2018; Hadd and Lahbiri, 2022), one can model more complex phenomena, such as population fluctuations, which result from age-dependent decay and growth, and potentially such models could also be used to model the growth lag.

DOM plays a key role in the carbon cycle in the oceans, and among others, it is one of the sources of energy for microheterotrophs (Dittmar et al., 2021). Yet, the composition of DOM differs and the ability of microorganisms to consume it also depends on the presence of other macronutrients. Near-surface waters are often nitrogen-, and phosphorous-limited (Moore et al., 2013), e.g., the northern Adriatic is P-limited (Grilli et al., 2020; Fanelli et al., 2022). A disruption of the nutrient balance may therefore start a succession of events. Biogeochemical models deal with such interplay of living organisms, and the chemistry of oceans (Vichi et al., 2007; BFM Consortium, 2024).

One largely overlooked source of organic matter in the ocean is gelatinous marine zooplankton (the cnidarian subphylum Medusozoans and phylum Ctenophore, hereinafter jellyfish). The amount of carbon stored in jellyfish in the epipelagic ocean was recently estimated to amount to $\sim 510 \times 10^9$ kg (Luo et al., 2020). Besides, due to their great ability to adapt, jellyfish might be the winners of the future ocean (Richardson et al., 2009). Adaptive features of jellyfish likely enable their proliferation under projected oceanic changes, such as warming, acidification, oxygen loss, and the increasing human exploitation of its ecosystem services (Richardson et al., 2009; Purcell, 2012; Steinberg and Landry, 2017). Despite debates on the cause of recent jellyfish population fluctuations, the increase of their numbers, influenced by natural population oscillations, anthropogenic stressors, and climate change, poses significant socioeconomic and serious ecological consequences (Richardson et al., 2009; Purcell, 2012; Condon et al., 2013; Sanz-Martín et al., 2016). In the aftermath, jellyfish blooms represent a considerable, but underappreciated source of organic matter, especially locally and regionally. Our previous findings indicate that decaying jellyfish blooms exhibit a distinct chemical and metabolic fingerprint compared to decaying phytoplankton blooms, potentially altering marine system functioning and biogeochemistry (Tinta et al., 2020, 2023; Fadeev et al., 2024). Namely, about half of jelly-OM is instantly available as DOM, which is rapidly respired and incorporated into the biomass by opportunistic bacteria. In less than 2 days jelly-OM degrading microbial consortia degraded most of jellyfish-derived proteins and amino acids. As the end result of microbial degradation of jelly-OM, substantial accumulation of ammonium and phosphate was recorded, with potentially important implications on biogeochemical cycles (Tinta et al., 2021; Fadeev et al., 2024). Currently, comprehensive experimental data sets on microbial degradation of jelly-OM are available only for a limited number of jellyfish species from a few marine ecosystems at restricted spatial–temporal scales. However, due to aforementioned characteristics of jelly-OM it is important to incorporate jellyfish into ocean biogeochemical models as key components of the biological soft-tissue pump (Steinberg and Landry, 2017; Lebrato et al., 2019). In order to comprehensively understand the importance of jellyfish–microbes interactions for biogeochemical cycles in the ocean, we need to expand our data sets by taking into account great jellyfish diversity, range of marine ecosystems and possible future scenarios of jellyfish population increase. One way to approach the great complexity of this problem is to create physical model of the jelly-OM microbial degradation process.

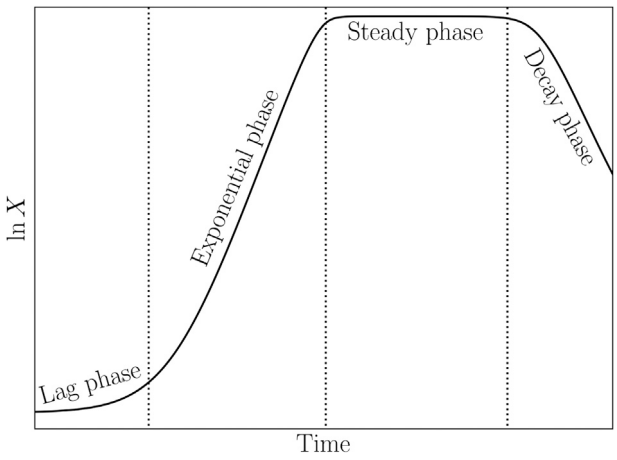

Fig. 1. A sketch of bacterial growth phases. $\ln X$ is the natural logarithm of the bacterial biomass.

In this work we present a bacterial population model based on the von Foerster equation with SIR-type model for kill-the-winner population decay. The model is developed for the purpose of describing a set of experiments where decaying jellyfish biomass is consumed by bacteria. During the process inorganic nutrients are released, which is described by the Luedeking–Piret equation. A system of equations, representing the model, is given, and its free parameters are adjusted to fit to the experimental data. The experimental data in question are laboratory microcosm experiments of two jellyfish species' decay in the northern Adriatic Sea. Finally, the results of these fits are discussed. The presented model does not deal with the full complexity of biogeochemistry of the ocean, but rather with a specific short-timescale seasonal event. As such it may present itself useful as a part of a multi-scale analysis of the biogeochemistry.

2. Material and methods

2.1. Model

Microorganisms subjected to a limited amount of substrate in a closed environment usually follow a typical growth-curve, which can be broken down in several phases (Fig. 1). For simplicity let us consider only the following:

1 lag phase;
2 exponential growth phase;
3 stationary or steady phase;
4 decay phase.

The lag phase occurs due to microorganisms adjusting to the environmental factors or the substrate (Rochman et al., 2016), but it is generally not well understood (Rolfe et al., 2012). Once adjusted,

the microorganisms start multiplying exponentially, entering the exponential growth phase, which lasts while the substrate is plentiful, and the environmental conditions are favorable. When the substrate starts running out the growth slows down, and eventually stands still, as the microbial population stabilizes in the stationary phase. Eventually this population can no longer be sustained in given conditions due to diverse factors: metabolite build-up, and consequent population poisoning, viral infection of the population (kill the winner) or changed environmental factors such as oxygen concentration, temperature or water pH. This results in the population entering the decay phase.

To model the exponential growth of bacteria we use the Monod's growth model, which is widely used in biogeochemical models:

$$\frac{\mathrm{d}X}{\mathrm{d}t} = \mu X, \tag{1}$$

$$\mu = \mu_{max}\frac{S}{K_S + S}, \tag{2}$$

where X is the biomass concentration, μ and μ_{max} are the specific growth rate and the maximal specific growth rate, respectively, S is the substrate concentration, and K_S is the biomass' affinity for the substrate. This model reproduces the sigmoid growth curves of the exponential growth, and stationary phases. During exponential growth the substrate consumption by microorganisms is modeled *via* the following correlation:

$$\frac{\mathrm{d}S}{\mathrm{d}t} = -\frac{\mu X}{Y_{X/S}}. \tag{3}$$

$Y_{X/S}$ is the biomass yield per unit of substrate consumed. To monitor (side-)product formation the Luedeking–Piret equation is used:

$$\frac{\mathrm{d}P}{\mathrm{d}t} = \alpha\mu X + \beta X, \tag{4}$$

where α relates to the product formation due to biomass growth, and β to the product formation due to respiration.

Eqs. (1)–(4) are a system of equations which we solve to describe microbial growth, as well as substrate consumption, and product formation during the exponential growth, and the stationary phases. They, however, fail to describe the lag phase. The latter we model with the von-Foerster-type equation (M'Kendrick, 1925; von Foerster et al., 1960), which assumes age-dependent growth rate. Age-dependent growth rate is supported by some studies (Stewart et al., 2005; Lavric and Graham, 2010; Stukalin et al., 2013; Rochman et al., 2018), but maturity is also sometimes used instead of age (Hadd and Lahbiri, 2022). The previous system of equations thus becomes:

$$X(t) = \int_0^\infty x(\tau,t)\mathrm{d}\tau, \tag{5}$$

$$\frac{\partial x}{\partial t} + \frac{\partial x}{\partial \tau} = -\mu(\tau)x(\tau,t), \tag{6}$$

$$x(0,t) = 2\int_0^\infty \mu(\tau)x(\tau,t)\mathrm{d}\tau, \tag{7}$$

$$\frac{\mathrm{d}S}{\mathrm{d}t} = -\frac{\int_0^\infty \mu(\tau)x(\tau,t)\mathrm{d}\tau}{Y_{X/S}}, \tag{8}$$

$$\frac{\mathrm{d}P}{\mathrm{d}t} = \alpha\int_0^\infty \mu(\tau)x(\tau,t)\mathrm{d}\tau + \beta X, \tag{9}$$

$$\mu(\tau) = \mu_{max}\exp\left(-k_\mu\tau\right)\frac{S}{K_S + S}. \tag{10}$$

τ represents the population's age, i.e. clock-time since last division, and x is the age density of the biomass. The latter can be thought of as a measure of the abundance of X of certain age (τ) and is related to X *via* Eq. (5). The assumption of fading specific growth rate introduces exponential decay into the calculation of μ, which contains an aging coefficient k_μ. Eqs. (6) and (7) assume that with each division 2 new cells appear, so the old cell is removed from the respective balance. In Eq. (10) we assume that with increasing age the specific growth rate follows an exponential decay function, which mostly affects the initial growth rate and thus introduces a lag phase. Eq. (6) can be further modified to also accommodate the decay phase:

$$\frac{\partial x}{\partial t} + \frac{\partial x}{\partial \tau} = -\left(\mu(\tau) + d\right)x(\tau,t). \tag{11}$$

The newly introduced coefficient d represents the specific decay rate. d can depend on environmental factors, toxin concentrations or even colony's age (Zahariev et al., 2015). A specific mode of colony decay is the "kill the winner" (KTW) event, where a viral infection spreads among the most populous bacteria in a community (Thingstad and Lignell, 1997). As a viral infection it can be modeled with SIR-type population models (i.e., *Susceptible, Infected, Removed*). We expand the existing model by introducing a population of infected bacteria I.

$$\frac{\mathrm{d}I}{\mathrm{d}t} = k_I\left(X - I\right)I - d_V I,\ \ X - I \geq 0. \tag{12}$$

Some studies model the viruses as a separate population (Miki and Yamamura, 2005), however, in the present study's SIR model, the population of viruses is not monitored separately, but is rather included within the infected population of bacteria. As the bacterial abundance is not modeled for separate bacterial strains, but is rather an umbrella term for all the present bacterioplankton, the outcome of the KTW model does not actually give a winning strain, as is otherwise the expected result (Miki and Yamamura, 2005; Maslov and Sneppen, 2017). The viral infection instead acts merely as a population ending event. In Eq. (12) k_I is the infection rate at which susceptible population is being infected, and d_V is the decay rate of the infected population. Per assumption, I behave the same as X up until the moment they die, and are equally present through all x. This eliminates the need for a separate variable for the susceptible population, which can be replaced by the difference $X - I > 0$. Consequently, d in (11) becomes $d = d_V I/X$, where I/X is the infected proportion of X. The decay may additionally affect the product balance, thus an extra term is added to the Luedeking–Piret equation to account for that:

$$\frac{\mathrm{d}P}{\mathrm{d}t} = \alpha\int_0^\infty \mu(\tau)x(\tau,t)\mathrm{d}\tau + \beta X + \gamma d_V I, \tag{13}$$

with γ being the coefficient related to product formation due to biomass decay.

To limit the upper age of x, τ_{max}, the following assumptions are applied:

$$\begin{aligned}\int_0^\infty x(\tau,t)\mathrm{d}\tau &= \int_0^{\tau_{max}} x(\tau,t)\mathrm{d}\tau + \int_{\tau_{max}}^\infty x(\tau,t)\mathrm{d}\tau\\ &= \int_0^{\tau_{max}} x(\tau,t)\mathrm{d}\tau + X_\infty,\\ \frac{\mathrm{d}X_\infty}{\mathrm{d}t} &= x(\tau_{max},t) - \mu_\infty X_\infty,\\ \int_0^\infty \mu(\tau)x(\tau,t)\mathrm{d}\tau &\approx \int_0^{\tau_{max}} \mu(\tau)x(\tau,t)\mathrm{d}\tau + \mu_\infty X_\infty.\end{aligned} \tag{14}$$

These assumptions can be made for τ_{max} large enough that the error of the following assumption is negligible: $\mu(\tau_{max}) \approx \mu_\infty$. They also simplify the numerical complexity of the problem, when solving Eqs. (5)–(10) discretely, as the discretization of the population's age then requires less variables (see Appendix A).

The system of equations presented above is made dimensionless by introducing the following variables: $\bar{X} = X/X^*$, $\bar{x} = x/X^*$, $\bar{I} = I/X^*$, $\bar{S} = S/S^*$, $\bar{P} = P/P^*$, with X^*, S^*, and P^* being constants (e.g., maximal experimental values of the respective variable). Additionally, some model constants need to be updated: $K'_S = K_S/S^*$, $Y'_{X/S} = Y_{X/S}S^*/X^*$, $\alpha' = \alpha X^*/P^*$, $\beta' = \beta X^*/P^*$, $\gamma' = \gamma X^*/P^*$, and $k'_I = k_I X^*$. Through these substitutions we arrive at the final model formulation:

$$\bar{X}(t) = \int_0^\infty \bar{x}(\tau,t)\mathrm{d}\tau, \tag{15}$$

$$\frac{\partial \bar{x}}{\partial t} + \frac{\partial \bar{x}}{\partial \tau} = -\left(\mu(\tau) + d_V\frac{\bar{I}}{\bar{X}}\right)\bar{x}(\tau,t), \tag{16}$$

$$\bar{x}(0,t) = 2\int_0^\infty \mu(\tau)\bar{x}(\tau,t)\mathrm{d}\tau, \tag{17}$$

$$\frac{\mathrm{d}\bar{S}}{\mathrm{d}t} = -\frac{\int_0^\infty \mu(\tau)\bar{x}(\tau,t)\mathrm{d}\tau}{Y'_{X/S}}, \tag{18}$$

$$\frac{\mathrm{d}\bar{P}}{\mathrm{d}t} = \alpha' \int_0^\infty \mu(\tau)\bar{x}(\tau,t)\mathrm{d}\tau + \beta'\bar{X} + \gamma' d_V \bar{I}, \tag{19}$$

$$\frac{\mathrm{d}\bar{I}}{\mathrm{d}t} = k'_I\left(\bar{X}-\bar{I}\right)\bar{I} - d_V\bar{I},\ \bar{X}-\bar{I}\geq 0, \tag{20}$$

$$\mu(\tau) = \mu_{max}\exp\left(-k_\mu\tau\right)\frac{\bar{S}}{K'_S+\bar{S}}. \tag{21}$$

The initial conditions, and the numerical procedures involved in solving this system of equations are further discussed in Appendix.

2.2. Experiments and fitting the model

The presented model is fitted to data from microcosm experiments in which we simulated the scenario potentially experienced by coastal pelagic microbial communities after the decay of a bloom of the cosmopolitan (*Aurelia aurita*) and invasive ctenophore (*Mnemiopsis leidyi*) in coastal marine ecosystems of the northern Adriatic Sea. For more details on these experiments see Tinta et al. (2020), Fadeev et al. (2024). Briefly, for each experiment we inoculated 1.2-μm-pre-filtered ambient prokaryotic coastal community collected in near-surface waters of the northern Adriatic Sea in aged seawater (ASW) media in a ratio of ASW:bacterial inoculum of 9:1. For each experiment, three of the experimental bottles received 100 mg of jellyfish or ctenophore dry matter L-1, representing the jelly-OM or cteno-OM treatment to mimic typical bloom conditions in a coastal ecosystem. Three experimental bottles remained unamended with jelly-OM and served as control. All bottles were incubated in the dark at *in situ* temperature (~24 °C) and mixed gently prior to subsampling. In all experiments, we sampled at short time intervals for bacterial abundance, dissolved organic carbon (DOC), total dissolved nitrogen (TDN), total hydrolyzed amino acids (TDHAA), dissolved free amino acids (DFAA) and inorganic nutrients (NH_4^+, PO_4^{3-}, NO_3^-, NO_2^-). In total we conducted and analyzed 2 experiments with *A. aurita* and 1 experiment with *M. leidyi* organic matter. Experiments were terminated at different stages of bacterial growth: one *A. aurita* experiment was terminated after bacterial community reached the late exponential phase (*A. aurita* exponential), and the other *A. aurita* and the *M. leidyi* experiments only after bacterial community entered decay phase (*A. aurita* full and *M. leidyi* full). At the same time, we analyzed the composition of bacterial community using microscopy-based and omic approach, but data were not used in this model and are discussed elsewhere (Tinta et al., 2020, 2023; Fadeev et al., 2024). Bacterial inoculum used in all our experiments was collected from the 5 m depth at the same sampling station and in the same season in the northern Adriatic Sea, but there was one year apart between *A. aurita* and *M. leidyi* experiments. Both *A. aurita* experiments were conducted using the same bacterial inoculum, which was sampled on the same day as the start of first experiment (*A. aurita* full) and was kept in the dark at 4 °C until used in the second experiment (*A. aurita* exponential) 4 days later. Results of these experiments are presented in Fig. 2.

As X we model the bacterial abundance, as S the concentration of the amino sulfonic acid taurine, and we additionally model two products of jelly-OM microbial degradation process P, namely ammonium and phosphate. Additionally, we model the change of dissolved organic carbon (DOC), as an independent substrate which is consumed during bacterial growth, but its concentration does not affect the growth rate. Although taurine cannot be considered the sole substrate for bacterial growth, and the process is likely more complex, it is used as a marker of DOM available for bacteria. As an amino sulfonic acid, taurine was one of the most abundant dissolved species picked-up in the analysis of free amino acids in the jelly-OM amino acid pool. Furthermore, taurine was available in great amount from the beginning, and was depleted during the experiment, unlike some other amino acids, as not all organic matter was processed during the microbial decay (Tinta et al., 2020). Ammonium ions are produced throughout the process of protein degradation (via ammonification, i.e., a process in which bacteria break down complex nitrogen-containing compounds to eventually ammonia), whereas phosphate ions appear to be depleting during the microbial growth, but are again being produced during stationary

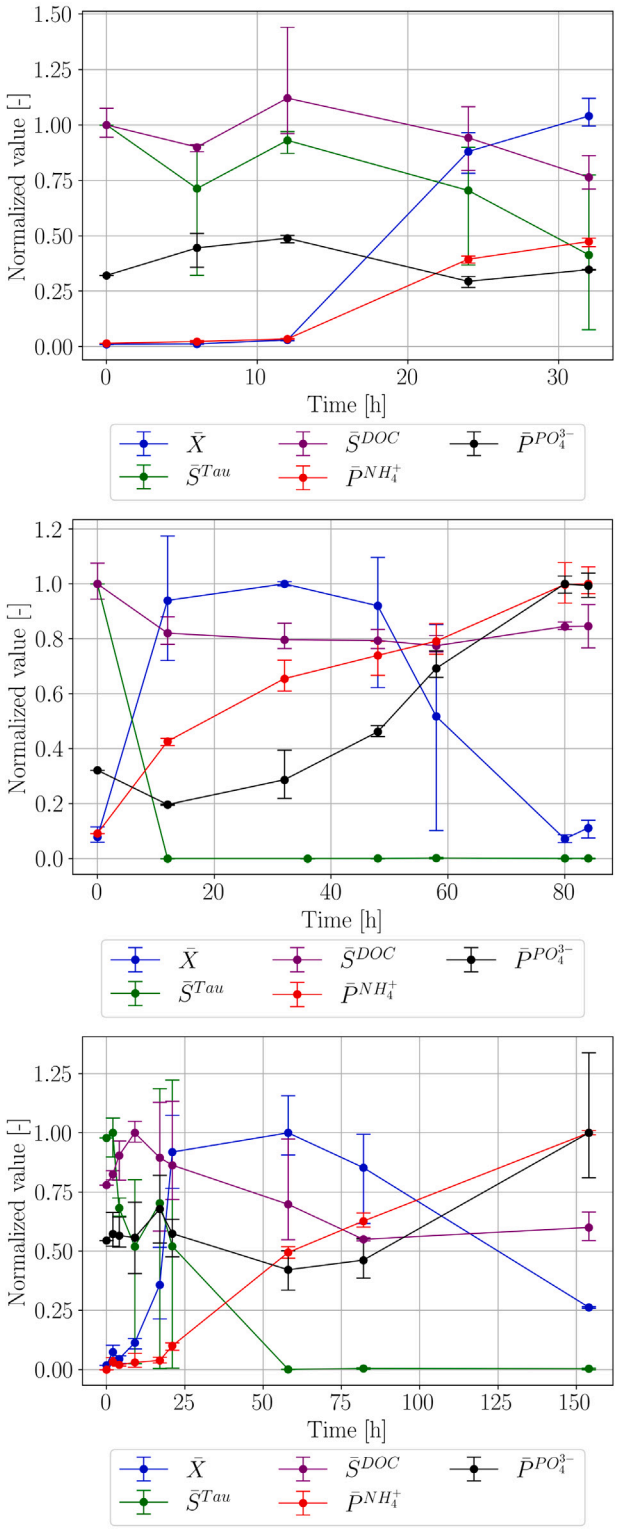

Fig. 2. Results of *A. aurita* exponential (top), *A. aurita* full (middle), and *M. leidyi* full (bottom) experiments. Shown are dimensionless values of bacterial abundance ($\bar{X}$), and concentrations of taurine ($\bar{S}^{Tau}$), DOC ($\bar{S}^{DOC}$), NH_4^+ ($\bar{P}^{NH_4^+}$), and PO_4^{3-} ($\bar{P}^{PO_4^{3-}}$).

growth phase, and even more so during the decay phase. *A. aurita* exponential results are used to find the model parameters of the exponential phase, and *A. aurita* full results are used to find the parameters of the steady, and decay phases. The model assumes constant environmental parameters such as pH, salinity, and temperature, as these were kept constant during experiments, and due to a relative short time-scale of the process (compared to oceanographic time-scales) it is likely that conditions would remain stable also in natural environments.

To fit the model to the experimental data, the following cost function λ is used:

$$\lambda = \sum_f \left[w_f \sum_i \left| 1 - \frac{f_{mod,i}}{f_{exp,i}} \right| \right], \tag{22}$$

where f represents model and experiment results (X, S, and P), w_f is the weight factor of f, indices mod, and exp represent the model and experiment, respectively, and i represents a common point in time, where an experimental measurement was made, and is compared to the model's values. w_f is equal to 1 when parameters related to f are being fitted, otherwise it equals 0.

The model is fitted to the experimental data by using the scipy's implementation of the differential evolution global optimizer (Virtanen et al., 2020). A cascaded approach is used for fitting the parameters, as they affect different parts of the model's output. This is done in order to reduce the computational complexity of the problem. Thus, parameters μ_{max}, K'_s, and k_{mu} are fitted first to the *A. aurita* exponential experiment, along with τ_m to adjust for a possible lag phase. $Y_{X/S}$ is assumed from the experimental data as the total amount of bacteria grown divided by the amount of substrate consumed. Then τ_m, k'_I, d_V, and ξ are fitted to the *A. aurita* full experiment. With this the bacterial growth and decay parameters are covered. The products-related parameters do not affect the growth phases, as no inhibition with products is present in the model. Therefore α', β', and γ' of each of the two products can be fitted separately, however as α' is related to the growth phase, it is fitted to the *A. aurita* exponential experiment, and the latter two parameters to the *A. aurita* full experiment. As we assume that DOC is consumed mostly during the growth phase, it was fitted to the *A. aurita* exponential experiment. Additionally, τ_m and ξ are free parameters, and are case/experiment specific, and are thus always optimized for each case.

Obtained parameters are then tested against the *M. leidyi* full experiment results, and adjusted, where required. It should be noted at this point that the experimental conditions, while controlled, were not entirely identical in both cases, therefore the *A. aurita* experiments cannot be entirely used to predict the behavior of the *M. leidyi* experiment. The starting community is likely different, and so is the composition of the substrate (Fadeev et al., 2024). Experiments were conducted one year apart, yet the community composition at the peak of bacterial abundance is very much the same, as shown through a metagenomic analysis (Fadeev et al., 2024). Both *A. aurita* experiments are indeed comparable, as the samples for them were collected at the same time.

All fitting procedures were done with $\Delta t = 1 \times 10^{-2}$ h, $\Delta\tau = 1 \times 10^{-2}$ h and $\tau_{max} = 100$ h. The initial conditions, parameters, and scaling parameters are given in Table 1.

Table 1
Initial conditions for solving Eqs. (15)–(21) when fitting model parameters to the experimental results. The superscripts Tau, DOC, NH_4^+, and PO_4^{3-} represent taurine, dissolved organic carbon, amonium ions, and phosphate ions, respectively.

	A. aurita exponential	*A. aurita* full	*M. leidyi* full
$\bar{X}_0$ [–]	0.078	0.011	0.019
$\bar{S}_0^{Tau}$ [–]	1	1	0.98
$\bar{S}_0^{DOC}$ [–]	1	1.1	1
$\bar{P}_0^{NH_4^+}$ [–]	0.091	0.015	0
$\bar{P}_0^{PO_4^{3-}}$ [–]	0.32	0.32	0.54
τ_w [h]	50	50	50
σ_0 [h]	10	10	10
X^* [cells mL^{-1}]	1.1×10^7	1.1×10^7	7.8×10^6
S^{Tau*} [μmol L^{-1}]	2.3	2.3	0.82
S^{DOC*} [μmol L^{-1}]	126	126	180
$P^{NH_4^+*}$ [μmol L^{-1}]	27	27	16
$P^{PO_4^{3-}*}$ [μmol L^{-1}]	1.4	1.4	0.46

3. Results and discussion

Fig. 3 displays the model fitted to experimental data. Parameter values are listed in Table 2. Using the cascaded fitting procedure, described in the previous section, we obtained the bacterial growth parameters as well as parameters related to substrates consumption, and products formation. The exponential growth parameters, obtained by fitting the model to *A. aurita* exponential data, were used to model the growth phase of the *A. aurita* full experiment. The decay-related parameters were then obtained by fitting the model to *A. aurita* full results. These parameters were used as an initial guess when modeling the *M. leidyi* full experiment. Since good fits were obtained by using bacterial growth, and decay parameters (μ_{max}, k_μ, K_S, K_I, and d_V) these remained unchanged when fitting the model to *M. leidyi* full data. $Y_{X/S}^{Tau}$ varies from experiment to experiment, suggesting different growth efficiencies with regard to taurine, where *A. aurita* experiments show about twice the bacterial growth with regards to taurine. However, $Y_{X/S}^{DOC}$ suggests that bacteria in *M. leidyi* experiment consume DOC about twice less efficiently. In other words, the bacterial community exposed to *M. leidyi* was less efficient in using DOC for building up its biomass, but this was not also reflected in the efficiency of taurine consumption. There are two possible explanations for this: (i) difference in quality and quantity of substrate and (ii) different composition and performance of bacterial community in each experiment. Since we know that the bacterial community composition was remarkably similar between experiments with two different substrates, i.e., *A. aurita* and *M. leidyi* (Fadeev et al., 2024), and we added the same quantity of different substrates, the observed difference must be due to differences in available substrates quality. This is in line with our observations that the *A. aurita s.l.* contains more than twice the amount of dissolved organic carbon, total dissolved nitrogen, dissolved free amino acids and phosphate, as well as a higher amount of proteins, as compared to *M. leidyi* (Fadeev et al., 2024). Thus, *A. aurita* represent a higher quality substrate for marine bacteria compared to *M. leidyi*. Bacteria exposed to *A. aurita* have more substrate available to support growth of their biomass. This is in line with our experimental results, showing that the addition of *M. leidyi*-OM to the microcosms promoted rapid bacterial growth and activity, similar to the *A. aurita*-OM treatments (Tinta et al., 2020; Fadeev et al., 2024). However, the biomass reached by the bacterial communities in *M. leidyi*-OM microcosms was much lower compared to the *A. aurita s.l.* experiment, likely due to the higher DOC content of *A. aurita s.l.* (see Table 2).

It should be noted that leeching of DOC from decaying jellyfish is not included in the model, and therefore the highest measured DOC value from experiments was used as the initial condition of the model. This may explain the misfitting of the DOC model, which was predicted with *A. aurita* exponential data, on *A. aurita* full data. More DOC may have been released from particulate organic matter fraction in the time between the first two data points, and was thus unaccounted for.

Generally, the bacterial yield from a substrate accounts for all substrate consumed, even if it was not used directly towards the biomass growth (Cajal-Medrano and Maske, 1999), and the present model does not follow bacterial respiration separately. Nevertheless, model output parameters such as α and β provide information on product formation due to bacterial biomass growth and product formation as a result of bacterial respiration. Product formation was inconsistent between the *A. aurita* experiments, and the *M. leidyi* experiment. The fit obtained on the *M. leidyi* data suggests tenfold lower NH_4^+ production due to bacterial growth than in *A. aurita* experiments (parameter α_N). Production due to respiration is similar in both cases (parameter β_N),

Table 2
Final parameter values. Indices N and P represent ammonium and phosphate, respectively, and Tau and DOC superscripts represent taurine, and dissolved organic carbon, respectively.

Parameter	*A. aurita* exponential	*A. aurita* full	*M. leidyi* full
μ_{max} [h^{-1}]	0.36	0.36	0.36
k_μ [h^{-1}]	0.049	0.049	0.049
K_S [$\mu mol\ L^{-1}$]	0.10	0.10	0.10
K_I [h^{-1}]	6.4×10^{-8}	6.4×10^{-8}	6.4×10^{-8}
d_V [h^{-1}]	0.26	0.26	0.26
$Y_{X/S}^{Tau}$ [cells L μmol^{-1} mL^{-1}]	5.1×10^{6}	4.5×10^{6}	9.6×10^{6}
$Y_{X/S}^{DOC}$ [cells L μmol^{-1} mL^{-1}]	2.6×10^{5}	2.6×10^{5}	1.1×10^{5}
α_N [$\mu mol\ mL\ cell^{-1}\ L^{-1}$]	1.0×10^{-6}	1.0×10^{-6}	1.4×10^{-7}
β_N [$\mu mol\ mL\ cell^{-1}\ L^{-1}\ h^{-1}$]	1.4×10^{-8}	1.4×10^{-8}	2.0×10^{-8}
γ_N [$\mu mol\ mL\ cell^{-1}\ L^{-1}$]	5.1×10^{-7}	5.1×10^{-7}	2.5×10^{-7}
α_P [$\mu mol\ mL\ cell^{-1}\ L^{-1}$]	-7.1×10^{-9}	-7.1×10^{-9}	-7.95×10^{-9}
β_P [$\mu mol\ mL\ cell^{-1}\ L^{-1}\ h^{-1}$]	1.7×10^{-10}	1.7×10^{-10}	8.4×10^{-12}
γ_P [$\mu mol\ mL\ cell^{-1}\ L^{-1}$]	9.0×10^{-8}	9.0×10^{-8}	4.4×10^{-8}
τ_m [h]	96.9	75.6	89.0
ξ [–]	0	6.3×10^{-8}	1.0×10^{-4}

and the release of NH_4^+ during the decay phase is about half in the *M. leidyi* experiment than in the *A. aurita* experiments (parameter γ_N). The release of ammonia is the end product of ammonification, i.e., a process in which bacteria break down complex nitrogen-containing compounds, like proteins. High release rate of ammonia (production) thus implies a higher rate of protein degradation by bacteria. In other words, based on our model outputs, supported with our experimental data, it seems that bacterial community exposed to *M. leidyi* had much less proteins available to degrade and support its biomass growth (α_N). At the same time, similar β_N values for the *A. aurita*- as well as the *M. leidyi*-exposed community imply that the amount of ammonia produced is a result of bacterial respiration or maintenance of basic metabolism. Both *A. aurita* and *M. leidyi* support similar rates of bacterial respiration of basic metabolism. This is in line with our previous observations that the *M. leidyi* degrading community exhibits lower bacterial growth efficiency (BGE) than *A. aurita* degrading communities (Tinta et al., 2020; Fadeev et al., 2024). Lower BGE implies that bacteria incorporate less carbon into their biomass but use it mainly for respiration or basic bacterial metabolism maintenance. BGE of bacterial communities is an important parameter, which helps us understand if carbon from a specific source is either more respired (low BGE) and thus lost for the ecosystem (as CO_2) or incorporated into bacterial biomass (high BGE) and thus retained in the food web (e.g., propagated in the food chain when bacteria are grazed or used by other microorganism upon bacterial lysis). Finally, the discrepancy in the rate of release of ammonia during the decay phase (γ_N) could be interpreted as less nitrogen being incorporated into the bacterial biomass during the growth phase, and similarly less of it being available for release upon its decay.

According to the fitted results, the consumption of PO_4^{3-} during the growth phase is similar among all the experiments (α_P), the production due to respiration (β_P) is negligible in the *M. leidyi* experiment, and about 20-times higher in *A. aurita* experiments, yet still minimal, and the release of PO_4^{3-} during the decay phase (γ_P) is halved for the *M. leidyi* experiment as compared to *A. aurita* experiments. This output is again in line with our hypothesis, also supported by experimental data, that bacterial community exposed to *A. aurita* was characterized by higher biomass growth, which is energetically a very expensive process and requires more phosphate. The fact that in the exponential growth both communities were consuming phosphate with similar rates can be explained by the fact that the studied coastal ecosystem, where we sampled the bacterial inoculum, is P-depleted, hence the ambient community is P-starved. The higher release rate of phosphate during decay of *A. aurita*-degrading community can probably be explained by the fact that in the *A. aurita* experiment the bacterial community decayed rapidly, probably due to a viral attack. Once this highly abundant community with high biomass crashed, more phosphate contained in their cells was released into the system. At this stage, all free phosphate released from jelly-OM was consumed and the remaining community had to make use of P stored in organophosphorus compounds. The

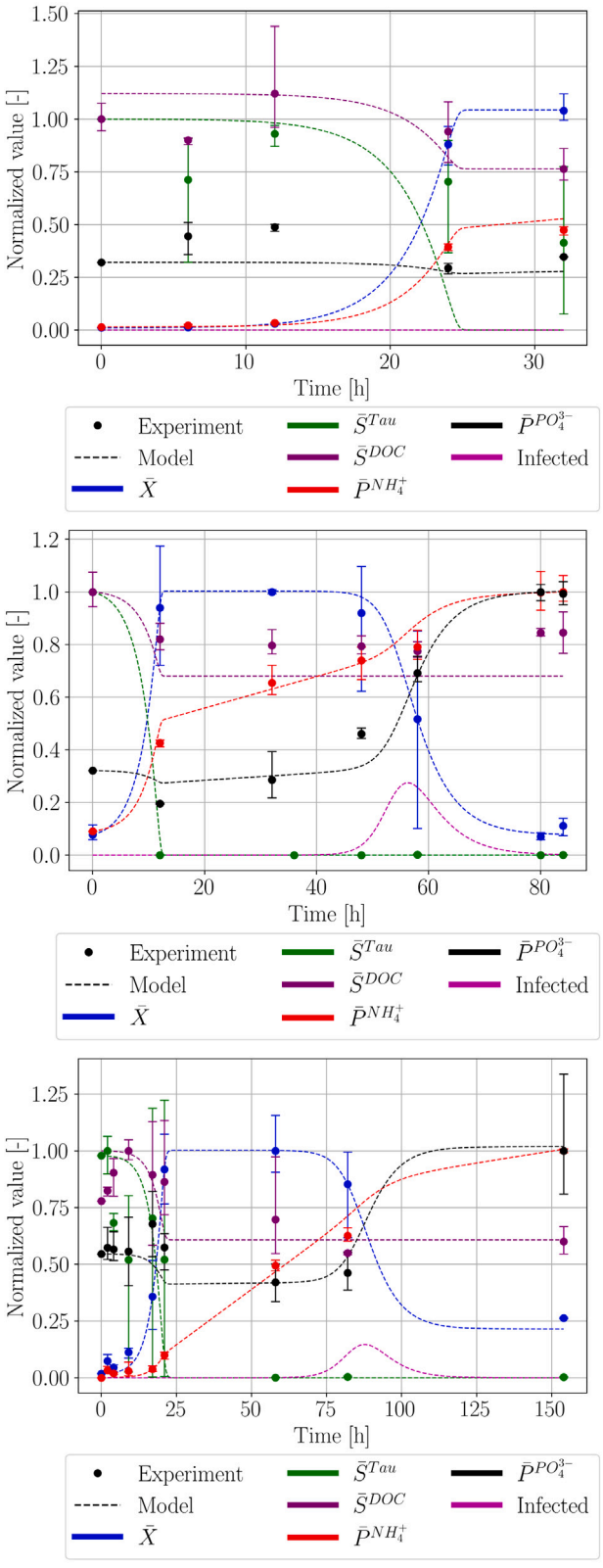

Fig. 3. Model and experiments comparison for the *A. aurita* exponential case (top); *A. aurita* full case (middle); *M. leidyi* full (bottom).

phosphate measured in the system is probably the end result of extracellular alkaline phosphate activity, released by bacteria during decay phase (Tinta et al., 2023).

Model parameters that describe the bacterial community (μ_{max}, k_μ, K_S, K_I, and d_V) are identical between the *A. aurita* and *M. leidyi* fits. This compatibility of bacterial growth and decay parameters suggests similarity of the bacterial populations in the experiments, as well as a similar mode of their decay. There was apparently a higher viral presence in the sample collected for the *M. leidyi* experiment, but this claim is based on model fits, as experiments did not monitor viruses. The bacterial production was seemingly more efficient per unit of taurine consumed, but this rather suggests that taurine is likely not the most suitable tracer of DOC available to marine bacteria or other parameters may affect general growth efficiency. The latter is beyond the scope of this paper, as we do not have sufficient data points to investigate correlations with environmental parameters further, but e.g., varying concentrations of inorganic nutrients in the environment may affect the growth-to-respiration ratios of bacterioplankton (Shchur et al., 2004). Interestingly, both NH_4^+ and PO_4^{3-} release during the decay phase is twice as high in the *A. aurita* than in the *M. leidyi* experiment. Nevertheless, the released inorganic nutrients, as the end results of microbial degradation of jelly-OM, represent a major nutrient input, particularly in oligotrophic environments, with possible implications for biogeochemical cycles and primary production.

The first order decay function for specific growth rate is used in this study for its simplicity, and differently shaped functions were not studied. Additionally, the viral infection susceptibility of cells is not cell-age dependent in the proposed model, as this would introduce yet more parameters. The proposed model is meant mainly as a means of analyzing laboratory results, as it has the ability to capture the whole life cycle of a bacterial community. With its need to track several discrete age densities, it is impractical for large-scale biogeochemical simulations, as simulating the transport of thousands of tracers would be computationally too expensive. As such it would be the most appropriate to use the model as a piece in the mosaic of a multi-scale model. Alternatively, the proposed model can be simplified by removing the cell-age component, as its main function is to model the growth lag, which is only relevant for experimental studies.

4. Conclusion

The developed model offers an insight into several stages of microbial-mediated degradation processes of jellyfish detritus released during collapse of the bloom. Through several growth-, and decay-related parameters it describes the life cycle of an ambient microbial community exposed to jellyfish-derived organic matter, and through growth yield parameters it describes the community's ability to turn a substrate into biomass. It also captures the production of respiration and remineralization products, specifically in this study the ammonia and phosphate. The proposed model is applied and fitted to two sets of experiments, analyzing the effect of a collapse of blooms of two different groups of gelatinous zooplankton — ctenophore *M. leidyi* and jellyfish *A. aurita* - on the ambient marine microbial community. Previous studies, dealing with the experiments, as well as the interpretation of model fits presented here, suggest certain discrepancies between the two organic matter sources. *A. aurita* experiments show that *A. aurita* organic matter is more favorable for bacterioplanktonic growth than *M. leidyi* organic matter, and consequently yields greater bacterial abundance at its peak. However, in both cases the resultant bacterial community is very similar, which is shown also through model fits, namely the bacterial growth, and decay parameters that fit the model to *A. aurita* experiments are the same as for *M. leidyi* experiment. The developed model can be eventually used to extend the current biogeochemical models (e.g., BFM Consortium, 2024) and coupled with ocean circulation models to understand the effect of jellyfish blooms, specifically in terms of organic matter released as jellyfish populations decay, on the natural microbial community and thus, on marine ecosystem functioning and biogeochemical cycles in the ocean. In particular, the invasive bloom-forming ctenophore as perturbation and the potential new, sporadically available, source of DOM for the natural bacterial community of the invaded coastal marine ecosystem are interesting. The resulting modeling system could be also used to perform case studies in realistic spatial and temporal context and provide a solid base for further development into a prognostic system capable of forecasting the system response to anthropogenic and natural perturbations in the coastal marine ecosystems affected by potentially increasing jellyfish blooms in the future. Nevertheless, there are still some technical challenges that have to be addressed before one can design a proposed modeling system that are mostly related to the numerical stability of the coupled multi-scale model.

CRediT authorship contribution statement

Filip Strniša: Writing – original draft, Visualization, Methodology, Investigation, Formal analysis, Conceptualization. **Tinkara Tinta:** Writing – original draft, Methodology, Funding acquisition, Conceptualization. **Gerhard J. Herndl:** Writing – review & editing. **Gregor Kosec:** Writing – review & editing, Supervision.

Declaration of competing interest

The authors declare that they have no known competing financial interests or personal relationships that could have appeared to influence the work reported in this paper.

Data availability

A juPyter notebook with an interactive implementation of the presented model is available at https://gitlab.com/e62Lab/public/2024_p_jellyfish_decay_example_code. The notebook also contains the necessary data to recreate the graphs from the Results section. More data for the modeled experiments can be found in respective original publications (Tinta et al., 2020; Fadeev et al., 2024).

Acknowledgments

This project was supported by the Slovenian Research Agency under grant number ARRS J7-2599, and by Research Core Funding P2-0095 and P1-0237. TT received further funding from the European Union's Horizon 2020 Research and Innovation Program under the Marie Skłodowska-Curie Grant Agreement No. 793778. GJH received funding by the FWF, Austria grant number I 4978-B. The contributions by Luka Jože Pušlar to the Python code are acknowledged. We thank dr. Katja Klun and Barbara Mähnert for help with chemical analyses. We also thank Alvaro Escobar and Jennifer H. Hennenfeind and Chie Amano for their help with microscopy-based analyses.

Appendix A. Discretization and stability conditions

The system of Eqs. (15)–(21) is solved numerically with the finite difference method, and Euler time-integration. We introduce the finite difference:

$$\frac{\partial \bar{x}(\tau,t)}{\partial \tau} = \frac{\bar{x}(\tau,t) - \bar{x}(\tau-\Delta\tau,t)}{\Delta\tau} + O(\Delta\tau) = \frac{\bar{x}_{a,i} - \bar{x}_{a-1,i}}{\Delta\tau} + O(\Delta\tau). \tag{A.1}$$

The integrals in Eqs. (15), (17), (18), and (19) are computed with the trapezoid method (trap) (Sirca and Horvat, 2012; Virtanen et al., 2020) in bounds $0 \le \tau \le \tau_{max}$, where τ_{max} should be greater than the maximum analyzed time t_{max}. By applying the Euler method, and the assumptions above, Eqs. (15)–(21) are transformed into the following system:

$$\bar{X}_i = \mathrm{trap}(\bar{x}_i(\tau),\tau)\big|_0^{\tau_{max}}, \tag{A.2}$$

$$\bar{x}_{a,i+1} = \bar{x}_{a,i} + \frac{\Delta t}{\Delta \tau}\left(\bar{x}_{a-1,i} - \bar{x}_{a,i}\right) - \Delta t\left(\mu + d_V \frac{\bar{I}}{\bar{X}}\right)\bar{x}_{a,i}, \tag{A.3}$$

$$\bar{x}_{0,i+1} = 2\mathrm{trap}(\mu(\tau)\bar{x}_i(\tau), \tau)|_0^{\tau_{max}}, \tag{A.4}$$

$$\bar{S}_{i+1} = \bar{S}_i - \frac{\Delta t}{Y'_{X/S}}\frac{\bar{x}_{0,i+1}}{2}, \tag{A.5}$$

$$\bar{P}_{i+1} = \bar{P}_i + \Delta t\left(\alpha' \frac{\bar{x}_{0,i+1}}{2} + \beta' \bar{X}_i + \gamma' d_V \bar{I}_i\right), \tag{A.6}$$

$$\bar{I}_{i+1} = \bar{I}_i + \Delta t\left[k'_I\left(\bar{X}_i - \bar{I}_i\right)\bar{I}_i - d_V \bar{I}_i\right], \ \bar{X}_i - \bar{I}_i \geq 0, \tag{A.7}$$

$$\mu(\tau) = \mu_{max} \exp\left(-k_\mu \tau\right) \frac{\bar{S}_i}{K'_S + \bar{S}_i}. \tag{A.8}$$

This system is solved with the following set of initial conditions:

$$\begin{aligned} &\bar{x}(\tau, t=0) = f(\tau), \ \mathrm{trap}(f(\tau), \tau)|_0^{\tau_{max}} = \bar{X}_0, \\ &\bar{S}(t=0) = \bar{S}_0, \\ &\bar{P}(t=0) = \bar{P}_0, \\ &\bar{I}(t=0) = \xi \bar{X}_0, \end{aligned} \tag{A.9}$$

where ξ is the coefficient of viral presence in the colony, a quasi fraction of infected cells.

To obtain a stable solution of Eq. (A.3), the CFL condition $\Delta t/\Delta\tau \leq 1$ needs to be satisfied. Additionally, as the value of $\bar{S}$ becomes small ($\bar{S} \ll K'_S$), the solution of the system may become unstable. $\bar{X}$ usually reaches its maximum value at that point (all S is nearly depleted, growth slows down), Eq. (A.8) becomes:

$$\mu \approx \mu_{max} \exp\left(-k_\mu \tau\right) \frac{\bar{S}_i}{K'_S}, \ \bar{S}_i \ll K'_S, \tag{A.10}$$

and consequently:

$$\bar{S}_{i+1} = \bar{S}_i - \Delta t \frac{\mu_{max}}{Y'_{X/S} K'_S} \mathrm{trap}\left[\exp\left(-k_\mu \tau\right)\bar{x}_i, \tau\right]|_0^{\tau_{max}} \bar{S}_i, \ \bar{S}_i \ll K'_S. \tag{A.11}$$

The conditions described above are found at the beginning of the stationary growth phase. At that point:

$$\mathrm{trap}\left[\exp\left(-k_\mu \tau\right)\bar{x}_i, \tau\right]|_0^{\tau_{max}} \approx \max(\bar{X}). \tag{A.12}$$

Thus Eq. (A.11) is simplified to:

$$\bar{S}_{i+1} = \bar{S}_i - \Delta t \frac{\mu_{max} \max(\bar{X})}{Y'_{X/S} K'_S} \bar{S}_i, \ \bar{S}_i \ll K'_S. \tag{A.13}$$

The expression $\frac{\mu_{max}\max(\bar{X})}{Y'_{X/S}K'_S}$ is assumed to be constant and positive, and is replaced by c. Assuming a temporary initial condition $\bar{S}_0$ for Eq. (A.13), it can be shown that $\bar{S}_n$, a solution after n iterations, equals:

$$\bar{S}_n = \bar{S}_0 (1 - c\Delta t)^n, \ n \in \mathbb{N}. \tag{A.14}$$

From Eq. (A.14) follows that in order for the errors not to be amplified through iteration $|1 - c\Delta t| > 1$. Thus $c\Delta t > 0$, and since $c \in \mathbb{R}^+$, $\Delta t > 0$. Additionally, values of Δt that satisfy $-1 < 1 - c\Delta t < 0$ yield numerically stable, yet oscillating solutions, and if $\Delta t = \frac{1}{c}$, all solutions of Eq. (A.14) equal 0. However, since c is not truly constant, the latter scenario is unlikely, and since in this case $\bar{S}_i \ll K'_S$ damped oscillations would not necessarily greatly affect the solution. Therefore as a general rule of thumb $0 < \Delta t < \frac{2}{c}$ should be satisfied, from which follows:

$$0 < \Delta t < 2 \frac{K'_S Y'_{X/S}}{\mu_{max} \max(\bar{X})}. \tag{A.15}$$

As $Y'_{X/S}$ indicates the amount of $\bar{X}$ grown from S_0 it automatically regulates $\max(\bar{X})$. Additionally, in dimensionless formulation both formerly mentioned values are approximately equal to 1. With these assumptions, the stability criterion is updated to:

$$0 < \Delta t < 2 \frac{K'_S}{\mu_{max}}. \tag{A.16}$$

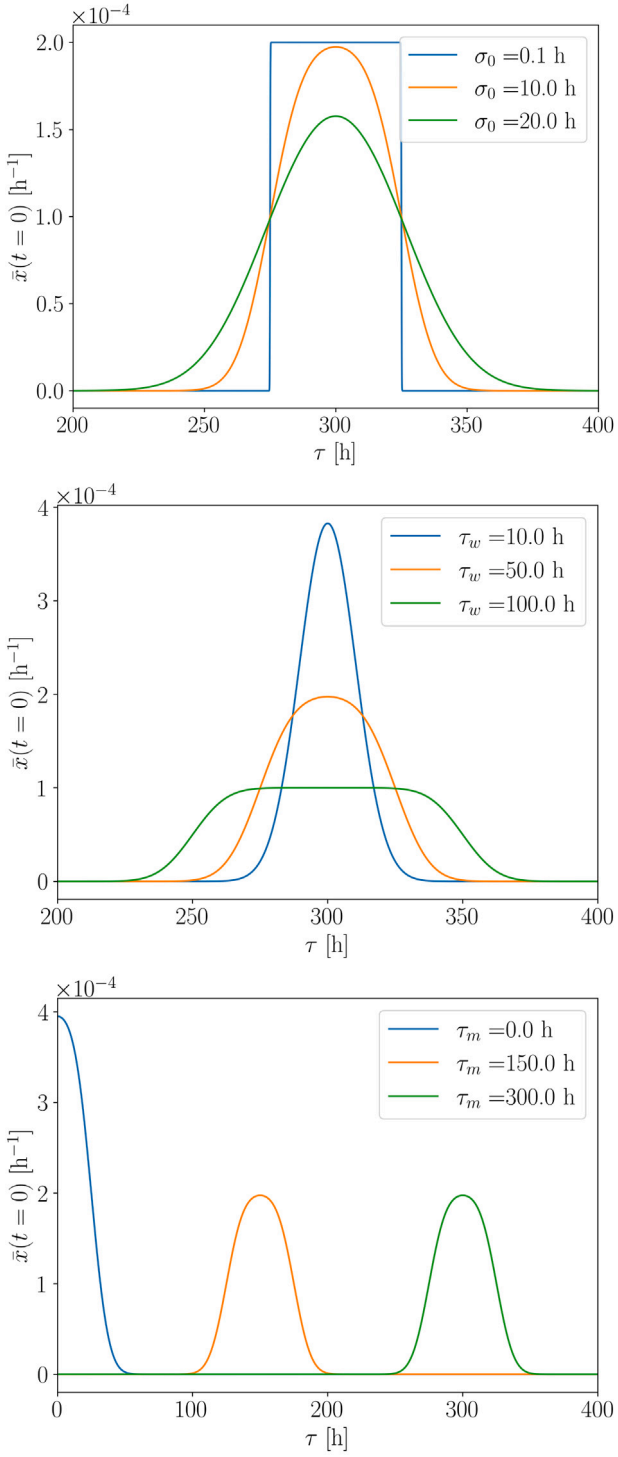

Fig. A.1. Effect of varying free parameters in Eq. (B.17) on initial distribution. From top to bottom: σ_0, τ_w, τ_m. Default settings that reproduce these curves are: $\tau_{max} = 600$ h, and unless differently specified $\sigma_0 = 10$ h, $\tau_w = 50$ h, $\tau_m = 300$ h.

Appendix B. Initial conditions

In Appendix A the initial conditions for solving Eqs. (A.2)–(A.8) are given by (A.9). The initial population distribution $\bar{x}(\tau, t = 0) = f(\tau)$ may affect the final solution. This is investigated by setting $f(\tau)$ to the

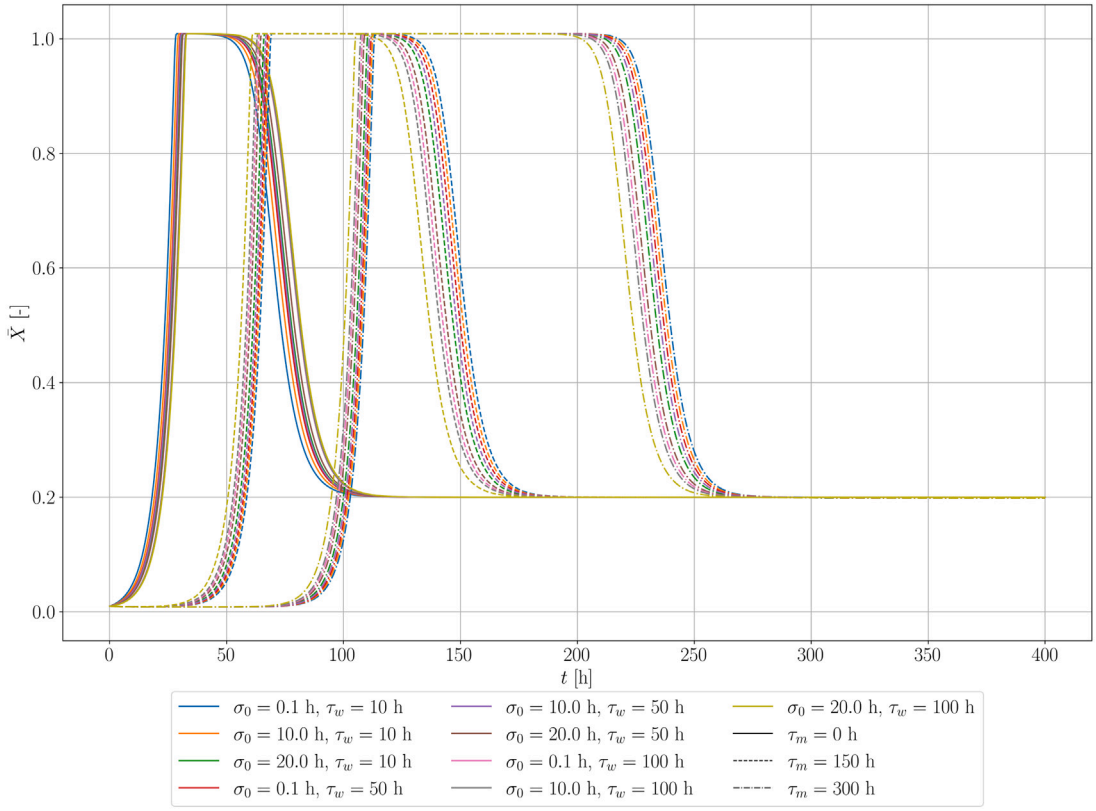

Fig. A.2. The effect of the initial distribution $\bar{x}(t = 0)$ on $\bar{X}(t)$ solution.

Table A.1
Eq. (B.17) settings that are tested. All available combinations of parameter values presented below are used, and their results analyzed.

Parameter	Value		
τ_m [h]	0	$\frac{\tau_{max}}{4}$	$\frac{\tau_{max}}{2}$
τ_w [h]	10	50	100
σ_0 [h]	0.1	10	20

Table A.2
Parameters and initial conditions for solving Eqs. (A.2)–(A.8) for analysis of initial distribution effects on the solution.

Parameter	Value	Initial condition	Value
μ_{max} [h^{-1}]	0.2		
K'_S [–]	0.02		
τ_{max} [h]	200	$\bar{X}_0$ [–]	0.01
$Y'_{X/S}$ [–]	1	ξ [–]	0.135
k_μ [h^{-1}]	0.05	$\bar{S}_0$ [–]	1
k'_I [h^{-1}]	0.5		
d_V [h^{-1}]	0.25		

following family of bell curves:

$$f(\tau) = \frac{N}{2}\left[\operatorname{erf}\left(\frac{\tau - \tau_m}{\sqrt{2}\sigma_0}\right) - \operatorname{erf}\left(\frac{\tau - \tau_m + \tau_w}{\sqrt{2}\sigma_0}\right)\right], \tag{B.17}$$

where N is a normalizing factor, such that $\operatorname{trap}(f(\tau), \tau)|_0^{\tau_{max}} = \bar{X}_0$ is satisfied, and is computed on the go. τ_m sets the bell curve's mid-point, τ_w regulates its width, and σ_0 its slope. Several combinations of these free parameters (Table A.1) are used to obtain diverse initial distributions $\bar{x}(t = 0)$. The effects of these parameters are illustrated in Fig. A.1. The initial distributions $\bar{x}(t = 0)$ generated with combinations of parameters given in Table A.1 are used to obtain solutions for $\bar{X}$ and $\bar{S}$ for $0 \le t \le 400$ h, with initial conditions, and model parameters given in Table A.2. For these solutions $\Delta t = 0.025$ h and $\Delta\tau = 0.05$ h are used.

Table A.3
Mean age $\bar{\tau}$, variance σ^2, skewness s of final distributions $\bar{x}(t = 400\,\text{h})$, and lag time τ_L.

τ_m [h]	τ_w [h]	σ_0 [h]	$\bar{\tau}$ [h]	σ^2 [h^2]	s [–]	τ_L [h]
		0.1	375.30	11.01	1.65	3.56
	10	10.0	374.27	10.99	1.65	4.57
		20.0	372.93	10.99	1.65	5.91
		0.1	373.46	10.99	1.65	5.38
0	50	10.0	373.15	10.99	1.65	5.69
		20.0	372.31	10.99	1.65	6.52
		0.1	371.19	10.98	1.65	7.64
	100	10.0	371.11	10.99	1.65	7.73
		20.0	370.81	10.99	1.65	8.02
		0.1	334.58	10.97	1.65	44.22
	10	10.0	335.32	10.97	1.65	43.48
		20.0	337.52	10.97	1.65	41.27
		0.1	335.98	10.97	1.65	42.82
150	50	10.0	336.72	10.97	1.65	42.08
		20.0	338.92	10.97	1.65	39.88
		0.1	339.73	10.97	1.65	39.07
	100	10.0	340.46	10.97	1.65	38.34
		20.0	342.63	10.97	1.65	36.17
		0.1	290.29	10.92	1.66	88.51
	10	10.0	291.03	10.92	1.66	87.77
		20.0	293.24	10.93	1.66	85.56
		0.1	291.69	10.93	1.66	87.11
300	50	10.0	292.43	10.93	1.66	86.37
		20.0	294.65	10.93	1.66	84.15
		0.1	295.45	10.93	1.66	83.35
	100	10.0	296.19	10.93	1.66	82.61
		20.0	298.40	10.93	1.66	80.40

Results are presented in Figs. A.2 and A.3, as well as Table A.3. By a first glance at the graphs in Figs. A.2 and A.3 it can be assumed that parameters σ_0, and τ_w mostly do not affect the solution, at least when it comes to the shape of the final distribution (Fig. A.3). Due to

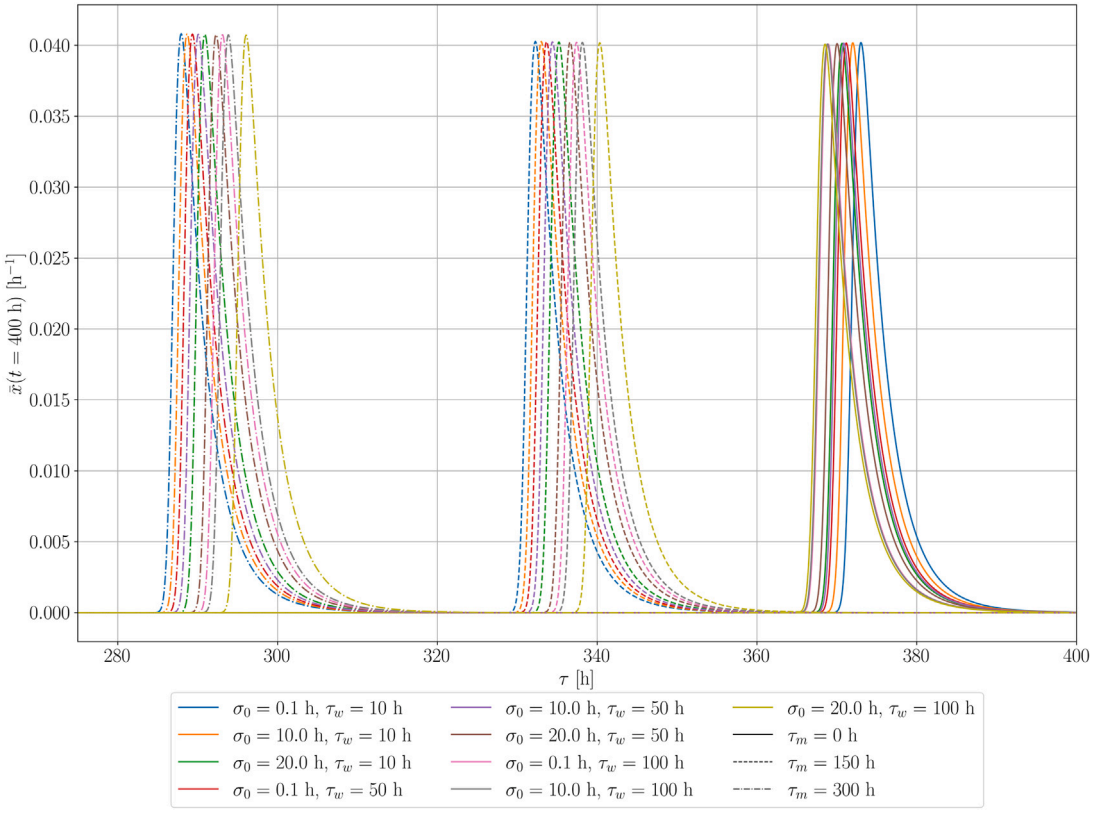

Fig. A.3. The effect of the initial distribution $\bar{x}(t = 0)$ on $\bar{x}(t = 400\,\text{h})$.

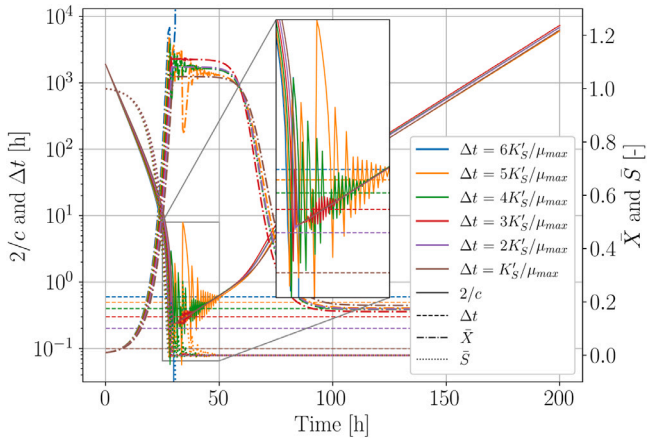

Fig. A.4. The stability constraint $2/c$ at different times t depicted with solid lines, where $c = \mu_{max}\frac{\text{trap}[\exp(-k_a\tau),\tau]}{K'_S+\bar{S}_i}$. Dashed lines represent Δt for comparison with the constraint. On the secondary axis are solutions of $\bar{X}$, and $\bar{S}$, depicted with dash-dotted, and dotted lines, respectively. The close-up is showing the $2/c$ and Δt comparison at the point where instabilities are expected in the solution.

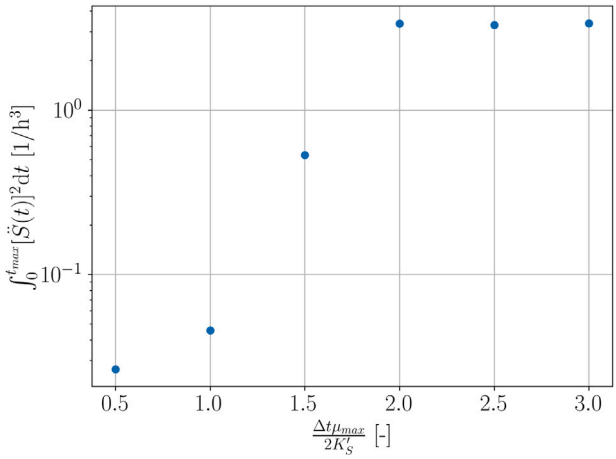

Fig. A.5. "Wigglyness" of the solution plotted against the quotient of Δt and the stability criterion approximation (Eq. (A.16)).

different initial age-distribution the aforementioned parameters may affect the initial growth lag, as is seen in Fig. A.2, although less so than τ_m affects it. These findings are further backed up by analyzing the final age distributions for their mean age, variance of the distribution, and its skewness as presented in Table A.3. The lag time therein is estimated by comparing the results to a non-population-based solution (Eqs. (1) and (3)). More precisely compared are the times each solution requires to reach $\bar{X} = 0.5$. Results show that combinations of σ_0, and τ_w within investigated ranges affect the lag time by a maximum of about 8 h, whereas varying τ_m gives us more control over lag time at specified model parameters. Results also show that all the final age distributions are qualitatively equal, as their variance and skewness are mostly the same. This age distribution shape is likely caused by the exponential growth phase, which is producing many young cells, and as the population ages once the substrate is depleted, the relative age structure remains the same. The latter quality is sometimes in literature referred to as "mean-scalable" (Rochman et al., 2018).

Appendix C. Stability and convergence

Appendix A briefly discusses the theoretical stability limits when solving Eqs. (A.2)–(A.8). These predictions are further tested in this

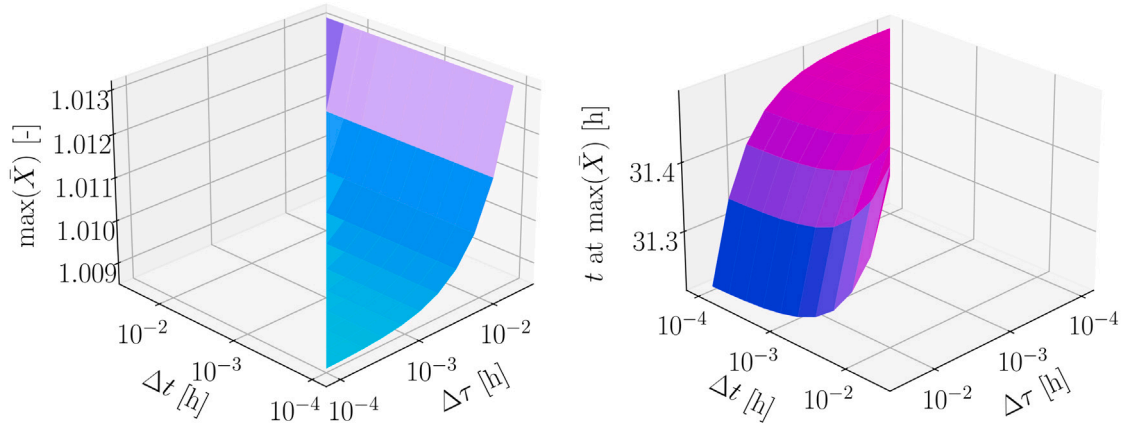

Fig. A.6. Convergence of the maximum $\bar{X}$ value max($\bar{X}$) (left) and its position in time (right). The plots were obtained by varying the age-distribution density $\Delta\tau$ and the integration time step Δt. Note different axes orientation in both plots. The CFL stability condition ($\frac{\Delta t}{\Delta\tau} \leq 1$) is well observable on both plots.

Table A.4
Parameters and initial conditions for solving Eqs. (A.2)–(A.8) for analysis of initial distribution effects on the solution, as well as solution stability, and system convergence.

Parameter	Value	Initial condition	Value
μ_{max} [h^{-1}]	0.2		
K'_S [–]	0.02		
τ_{max} [h]	200		
$Y'_{X/S}$ [–]	1	$\bar{X}_0$ [–]	0.01
k_μ [h^{-1}]	0.05	ξ [–]	0.135
k'_l [h^{-1}]	0.5	$\bar{S}_0$ [–]	1
d_V [h^{-1}]	0.25		
τ_m [h]	0		
τ_w [h]	50		
σ_0 [h]	10		

section. Eqs. (A.2)–(A.8) are solved with initial conditions given in Table A.4.

Solution stability is tested by varying Δt. As discussed previously, Eq. (A.16) suggests the stability bounds of Δt, therefore to test this prediction Δt is varied in the range: $\frac{K'_S}{\mu_{max}} \leq \Delta t \leq 6\frac{K'_S}{\mu_{max}}$. To satisfy the CFL condition in these tests $\Delta\tau$ is set to $2\Delta t$.

Furthermore, the assessment of the system's convergence is necessary. Initial conditions presented in Table A.4 are therefore used to solve the system with a range of Δt and $\Delta\tau$, namely $0.0001\,\text{h} \leq \Delta t,\ \Delta\tau \leq 0.025\,\text{h}$.

Fig. A.4 is displaying the change of the stability constraint (Eq. (A.15)) against time on the primary axis, and on the secondary axis the solutions of $\bar{X}$ and $\bar{S}$. Additionally, the values of Δt are also plotted on the primary axis. The closeup within the plot shows that instabilities in the solution occur for values of Δt where the dynamically changing stability constraint dips below said Δt. However, as the stability constraint starts growing after $\bar{S}$ is depleted a full solution may still be produced, and the system diverges only for the biggest Δt. The "wigglyness" of a function can be assessed by analyzing its changes in curvature. This can be done by integrating the second derivative of the function squared. Fig. A.5 displays a plot of "wigglyness" against the quotient of Δt and the stability criterion approximation (Eq. (A.16)). A significant increase of "wigglyness" can be seen once the criterion expressed in Eq. (A.16) is passed, which suggests that the solution gets less stable past that point.

The convergence tests are done for all combinations of Δt and $\Delta\tau$ from the following set {0.025, 0.014, 0.0082, 0.0047, 0.0027, 0.0016, 0.00090, 0.00052, 0.00030, 0.00017, 0.00010} h. Fig. A.6 is displaying the results of these tests. Plotted are maximal obtained values of $\bar{X}$, and times at which these maxima are found. Data where the CFL condition is violated are not displayed, as the solution diverges in those cases. The plot of maximal $\bar{X}$ suggests that this value is highly dependent on the value of $\Delta\tau$ which is in turn limited by the CFL condition. According to the times at which these maxima are found, the solution appears to converge the fastest when $\Delta\tau = \Delta t$. Although one should note that the deviation of times at maximum $\bar{X}$ is of the same magnitude as the high values of Δt and $\Delta\tau$.

References

Arndt, S., Jørgensen, B., LaRowe, D., Middelburg, J., Pancost, R., Regnier, P., 2013. Quantifying the degradation of organic matter in marine sediments: A review and synthesis. Earth-Sci. Rev. 123, 53–86. http://dx.doi.org/10.1016/j.earscirev.2013.02.008, URL: https://www.sciencedirect.com/science/article/pii/S0012825213000512.

Azam, F., Malfatti, F., 2007. Microbial structuring of marine ecosystems. Nat. Rev. Microbiol. 5 (10), 782–791. http://dx.doi.org/10.1038/nrmicro1747.

BFM Consortium, 2024. Biogeochemical flux model | BFM. bfm-community.eu. (Accessed 30 January 2024).

Cajal-Medrano, R., Maske, H., 1999. Growth efficiency, growth rate and the remineralization of organic substrate by bacterioplankton–revisiting the Pirt model. Aquat. Microb. Ecol. 19 (2), 119–128. http://dx.doi.org/10.3354/ame019119, URL: https://www.int-res.com/abstracts/ame/v19/n2/p119-128/.

Condon, R.H., Duarte, C.M., Pitt, K.A., Robinson, K.L., Lucas, C.H., Sutherland, K.R., Mianzan, H.W., Bogeberg, M., Purcell, J.E., Decker, M.B., ichi Uye, S., Madin, L.P., Brodeur, R.D., Haddock, S.H.D., Malej, A., Parry, G.D., Eriksen, E., Quiñones, J., Acha, M., Harvey, M., Arthur, J.M., Graham, W.M., 2013. Recurrent jellyfish blooms are a consequence of global oscillations. Proc. Natl. Acad. Sci. 110 (3), 1000–1005. http://dx.doi.org/10.1073/pnas.1210920110, arXiv:https://www.pnas.org/doi/pdf/10.1073/pnas.1210920110. URL: https://www.pnas.org/doi/abs/10.1073/pnas.1210920110.

Dittmar, T., Lennartz, S.T., Buck-Wiese, H., Hansell, D.A., Santinelli, C., Vanni, C., Blasius, B., Hehemann, J.-H., 2021. Enigmatic persistence of dissolved organic matter in the ocean. Nat. Rev. Earth Environ. 2 (8), 570–583. http://dx.doi.org/10.1038/s43017-021-00183-7.

Esser, D.S., Leveau, J.H.J., Meyer, K.M., 2015. Modeling microbial growth and dynamics. Appl. Microbiol. Biotechnol. 99 (21), 8831–8846. http://dx.doi.org/10.1007/s00253-015-6877-6.

Fadeev, E., Hennenfeind, J.H., Amano, C., Zhao, Z., Klun, K., Herndl, G.J., Tinta, T., 2024. Bacterial degradation of ctenophore *Mnemiopsis leidyi* organic matter. mSystems 9 (2), e01264–23. http://dx.doi.org/10.1128/msystems.01264-23, arXiv:https://journals.asm.org/doi/pdf/10.1128/msystems.01264-23. URL: https://journals.asm.org/doi/abs/10.1128/msystems.01264-23.

Fanelli, M., Girolametti, F., Truzzi, C., Illuminati, S., Ajdini, B., Susmel, S., Celussi, M., Šangulin, J., Annibaldi, A., 2022. Impact of depuration plants on nutrient levels in the north adriatic sea. Water 14 (12), http://dx.doi.org/10.3390/w14121930, URL: https://www.mdpi.com/2073-4441/14/12/1930.

Grilli, F., Accoroni, S., Acri, F., Bernardi Aubry, F., Bergami, C., Cabrini, M., Campanelli, A., Giani, M., Guicciardi, S., Marini, M., Neri, F., Penna, A., Penna, P., Pugnetti, A., Ravaioli, M., Riminucci, F., Ricci, F., Totti, C., Viaroli, P., Cozzi, S., 2020. Seasonal and interannual trends of oceanographic parameters over 40 years in the northern adriatic sea in relation to nutrient loadings using the emodnet chemistry data portal. Water 12 (8), http://dx.doi.org/10.3390/w12082280, URL: https://www.mdpi.com/2073-4441/12/8/2280.

Hadd, S., Lahbiri, F.Z., 2022. Stochastic delay-differential equations as bacterial population model with boundary feedback. IFAC-PapersOnLine 55 (12), 202–207. http://dx.doi.org/10.1016/j.ifacol.2022.07.312, URL: https://www.sciencedirect.com/science/article/pii/S2405896322007133. 14th IFAC Workshop on Adaptive and Learning Control Systems ALCOS 2022.

Hansell, D.A., Carlson, C.A., Repeta, D.J., Schlitzer, R., 2009. Dissolved organic matter in the ocean: a controversy stimulates new insights. Oceanography 22 (4), 202–211, URL: http://www.jstor.org/stable/24861036.

Lavric, V., Graham, D.W., 2010. Birth, growth and death as structuring operators in bacterial population dynamics. J. Theoret. Biol. 264 (1), 45–54. http://dx.doi.org/10.1016/j.jtbi.2010.01.020.

Lebrato, M., Pahlow, M., Frost, J.R., Küter, M., de Jesus Mendes, P., Molinero, J.-C., Oschlies, A., 2019. Sinking of gelatinous zooplankton biomass increases deep carbon transfer efficiency globally. Glob. Biogeochem. Cycles 33 (12), 1764–1783. http://dx.doi.org/10.1029/2019GB006265, arXiv:https://agupubs.onlinelibrary.wiley.com/doi/pdf/10.1029/2019GB006265. URL: https://agupubs.onlinelibrary.wiley.com/doi/abs/10.1029/2019GB006265.

Li, H., Xie, G., Edmondson, A., 2007. Evolution and limitations of primary mathematical models in predictive microbiology. Br. Food J. 109 (8), 608–626. http://dx.doi.org/10.1108/00070700710772408.

Luo, J.Y., Condon, R.H., Stock, C.A., Duarte, C.M., Lucas, C.H., Pitt, K.A., Cowen, R.K., 2020. Gelatinous zooplankton-mediated carbon flows in the global oceans: A data-driven modeling study. Glob. Biogeochem. Cycles 34 (9), e2020GB006704. http://dx.doi.org/10.1029/2020GB006704, arXiv:https://agupubs.onlinelibrary.wiley.com/doi/pdf/10.1029/2020GB006704. URL: https://agupubs.onlinelibrary.wiley.com/doi/abs/10.1029/2020GB006704. e2020GB006704 2020GB006704.

Maslov, S., Sneppen, K., 2017. Population cycles and species diversity in dynamic kill-the-winner model of microbial ecosystems. Sci. Rep. 7 (1), 39642. http://dx.doi.org/10.1038/srep39642.

McKellar, R., Lu, X. (Eds.), 2003. Modeling Microbial Responses in Food, first ed. CRC Press, http://dx.doi.org/10.1201/9780203503942.

McMeekin, T., Olley, J., Ratkowsky, D., Ross, T., 2002. Predictive microbiology: towards the interface and beyond. Int. J. Food Microbiol. 73 (2), 395–407. http://dx.doi.org/10.1016/S0168-1605(01)00663-8, URL: https://www.sciencedirect.com/science/article/pii/S0168160501006638. 3rd International Conference on Predictive Modelling in Foods.

Miki, T., Yamamura, N., 2005. Intraguild predation reduces bacterial species richness and loosens the viral loop in aquatic systems: kill the killer of the winner hypothesis. Aquat. Microb. Ecol. 40 (1), 1–12. http://dx.doi.org/10.3354/ame040001, URL: https://www.int-res.com/abstracts/ame/v40/n1/p1-12/.

M'Kendrick, A.G., 1925. Applications of mathematics to medical problems. Proc. Edinb. Math. Soc. 44, 98–130. http://dx.doi.org/10.1017/S0013091500034428.

Moore, C.M., Mills, M.M., Arrigo, K.R., Berman-Frank, I., Bopp, L., Boyd, P.W., Galbraith, E.D., Geider, R.J., Guieu, C., Jaccard, S.L., Jickells, T.D., La Roche, J., Lenton, T.M., Mahowald, N.M., Marañón, E., Marinov, I., Moore, J.K., Nakatsuka, T., Oschlies, A., Saito, M.A., Thingstad, T.F., Tsuda, A., Ulloa, O., 2013. Processes and patterns of oceanic nutrient limitation. Nat. Geosci. 6 (9), 701–710. http://dx.doi.org/10.1038/ngeo1765.

Peleg, M., Corradini, M.G., 2011. Microbial growth curves: What the models tell us and what they cannot. Crit. Rev. Food Sci. Nutr. 51 (10), 917–945. http://dx.doi.org/10.1080/10408398.2011.570463, arXiv:https://doi.org/10.1080/10408398.2011.570463. PMID: 21955092.

Purcell, J.E., 2012. Jellyfish and ctenophore blooms coincide with human proliferations and environmental perturbations. Annu. Rev. Mar. Sci. 4 (Volume 4, 2012), 209–235. http://dx.doi.org/10.1146/annurev-marine-120709-142751, URL: https://www.annualreviews.org/content/journals/10.1146/annurev-marine-120709-142751.

Richardson, A.J., Bakun, A., Hays, G.C., Gibbons, M.J., 2009. The jellyfish joyride: causes, consequences and management responses to a more gelatinous future. Trends Ecol. Evol. 24 (6), 312–322. http://dx.doi.org/10.1016/j.tree.2009.01.010, URL: https://www.sciencedirect.com/science/article/pii/S0169534709000883.

Rochman, N.D., Popescu, D.M., Sun, S.X., 2018. Ergodicity, hidden bias and the growth rate gain. Phys. Biol. 15 (3), 036006. http://dx.doi.org/10.1088/1478-3975/aab0e6.

Rochman, N., Si, F., Sun, S.X., 2016. To grow is not enough: impact of noise on cell environmental response and fitness. Integr. Biol. 8, 1030–1039. http://dx.doi.org/10.1039/C6IB00119J.

Rolfe, M.D., Rice, C.J., Lucchini, S., Pin, C., Thompson, A., Cameron, A.D.S., Alston, M., Stringer, M.F., Betts, R.P., Baranyi, J., Peck, M.W., Hinton, J.C.D., 2012. Lag phase is a distinct growth phase that prepares bacteria for exponential growth and involves transient metal accumulation. J. Bacteriol. 194 (3), 686–701. http://dx.doi.org/10.1128/jb.06112-11, arXiv:https://journals.asm.org/doi/pdf/10.1128/jb.06112-11. URL: https://journals.asm.org/doi/abs/10.1128/jb.06112-11.

Sanz-Martín, M., Pitt, K.A., Condon, R.H., Lucas, C.H., Novaes de Santana, C., Duarte, C.M., 2016. Flawed citation practices facilitate the unsubstantiated perception of a global trend toward increased jellyfish blooms. Global Ecol. Biogeogr. 25 (9), 1039–1049. http://dx.doi.org/10.1111/geb.12474, arXiv:https://onlinelibrary.wiley.com/doi/pdf/10.1111/geb.12474. URL: https://onlinelibrary.wiley.com/doi/abs/10.1111/geb.12474.

Shang, H., 2023. A generic hierarchical model of organic matter degradation and preservation in aquatic systems. Commun. Earth Environ. 4 (1), 16. http://dx.doi.org/10.1038/s43247-022-00667-4.

Shchur, L.A., Aponasenko, A.D., Lopatin, V.N., Makarskaya, G.V., 2004. The effect of mineral particulate matter on the productive characteristics of bacterioplankton and the degradation of labile organic material. Microbiology 73 (1), 84–88. http://dx.doi.org/10.1023/B:MICI.0000016374.72225.06.

Sirca, S., Horvat, M., 2012. Computational Methods for Physicists: Compendium for Students. In: Graduate Texts in Physics, Springer Berlin Heidelberg.

Steinberg, D.K., Landry, M.R., 2017. Zooplankton and the ocean carbon cycle. Annu. Rev. Mar. Sci. 9 (Volume 9, 2017), 413–444. http://dx.doi.org/10.1146/annurev-marine-010814-015924, URL: https://www.annualreviews.org/content/journals/10.1146/annurev-marine-010814-015924.

Stewart, E.J., Madden, R., Paul, G., Taddei, F., 2005. Aging and death in an organism that reproduces by morphologically symmetric division. PLoS Biol. 3 (2), http://dx.doi.org/10.1371/journal.pbio.0030045.

Stukalin, E.B., Aifuwa, I., Kim, J.S., Wirtz, D., Sun, S.X., 2013. Age-dependent stochastic models for understanding population fluctuations in continuously cultured cells. J. R. Soc. Interface 10, http://dx.doi.org/10.1098/rsif.2013.0325.

Thingstad, T., Lignell, R., 1997. Theoretical models for the control of bacterial growth rate, abundance, diversity and carbon demand. Aquat. Microb. Ecol. 13 (1), 19–27. http://dx.doi.org/10.3354/ame013019, URL: https://www.int-res.com/abstracts/ame/v13/n1/p19-27/.

Tinta, T., Klun, K., Herndl, G.J., 2021. The importance of jellyfish-microbe interactions for biogeochemical cycles in the ocean. Limnol. Oceanogr. 66 (5), 2011–2032. http://dx.doi.org/10.1002/lno.11741, arXiv:https://aslopubs.onlinelibrary.wiley.com/doi/pdf/10.1002/lno.11741. URL: https://aslopubs.onlinelibrary.wiley.com/doi/abs/10.1002/lno.11741.

Tinta, T., Zhao, Z., Bayer, B., Herndl, G.J., 2023. Jellyfish detritus supports niche partitioning and metabolic interactions among pelagic marine bacteria. Microbiome 11 (1), 156. http://dx.doi.org/10.1186/s40168-023-01598-8.

Tinta, T., Zhao, Z., Escobar, A., Klun, K., Bayer, B., Amano, C., Bamonti, L., Herndl, G.J., 2020. Microbial processing of jellyfish detritus in the ocean. Front. Microbiol. 11, 2638. http://dx.doi.org/10.3389/fmicb.2020.590995.

Vichi, M., Pinardi, N., Masina, S., 2007. A generalized model of pelagic biogeochemistry for the global ocean ecosystem. Part I: Theory. J. Mar. Syst. 64 (1), 89–109. http://dx.doi.org/10.1016/j.jmarsys.2006.03.006, URL: https://www.sciencedirect.com/science/article/pii/S0924796306001084. Contributions from Advances in Marine Ecosystem Modelling Research, 27-29 June, 2005, Plymouth, UK.

Virtanen, P., Gommers, R., Oliphant, T.E., Haberland, M., Reddy, T., Cournapeau, D., Burovski, E., Peterson, P., Weckesser, W., Bright, J., van der Walt, S.J., Brett, M., Wilson, J., Millman, K.J., Mayorov, N., Nelson, A.R.J., Jones, E., Kern, R., Larson, E., Carey, C.J., Polat, İ., Feng, Y., Moore, E.W., VanderPlas, J., Laxalde, D., Perktold, J., Cimrman, R., Henriksen, I., Quintero, E.A., Harris, C.R., Archibald, A.M., Ribeiro, A.H., Pedregosa, F., van Mulbregt, P., SciPy 1.0 Contributors, 2020. SciPy 1.0: Fundamental algorithms for scientific computing in python. Nat. Methods 17, 261–272. http://dx.doi.org/10.1038/s41592-019-0686-2.

von Foerster, H., Mora, P.M., Amiot, L.W., 1960. Doomsday: Friday, 13 november, A.D. 2026. Science 132 (3436), 1291–1295. http://dx.doi.org/10.1126/science.132.3436.1291, arXiv:https://www.science.org/doi/pdf/10.1126/science.132.3436.1291. URL: https://www.science.org/doi/abs/10.1126/science.132.3436.1291.

Wade, M., Harmand, J., Benyahia, B., Bouchez, T., Chaillou, S., Cloez, B., Godon, J.-J., Moussa Boudjemaa, B., Rapaport, A., Sari, T., Arditi, R., Lobry, C., 2016. Perspectives in mathematical modelling for microbial ecology. Ecol. Model. 321, 64–74. http://dx.doi.org/10.1016/j.ecolmodel.2015.11.002.

Zahariev, A., Kiskinov, H., Angelov, A., Zlatev, S., 2015. Time lag model for batch bioreactor simulation accounting the effect of micro-organism mortality. Biotechnol. Biotechnol. Equip. 29 (1), 195–199. http://dx.doi.org/10.1080/13102818.2014.993111, arXiv:https://doi.org/10.1080/13102818.2014.993111. PMID: 26019633.